FRONTIERS OF PHYSICS

RESEARCH ARTICLE
Volume 21 / Issue 12 / 124201 / 2026

Suppressing nucleation and slow-kinetic epitaxial growth of large domain 2D nonlayered β-In_2S_3 nanoflakes via water molecules for optoelectronic devices

Liqi He[1], Luwei Zou[1], Zian Li[1], Xiulian Fan[1], Chenyang Niu[1], Xilong Zhou[1], Cheng Li[1], Wenlong Chu[1], Huanzhi Chen[1], Yuqi Zou[1], Lin Mei[2], Yu Zhou[1,2,3,†]

1 School of Physics and Electronics, Hunan Key Laboratory of Nanophotonics and Devices, Central South University, Changsha 410083, China
2 State Key Laboratory of Powder Metallurgy, Central South University, Changsha 410083, China
3 State Key Laboratory of Precision Measuring Technology and Instruments, Tianjin University, Tianjin 300072, China
Corresponding author. E-mail: †yu.zhou@csu.edu.cn
Received January 22, 2026; accepted March 3, 2026

ABSTRACT

Nonlayered two-dimensional (2D) β-In_2S_3 nanostructures have demonstrated outstanding electronic and optoelectronic properties, which requires its large-scale single-crystalline films to suppress carrier scattering. However, the weak energy for In–S chemical bonds and inherent nonlayered structure with three dimensional bonds make it highly challenging to achieve large area 2D β-In_2S_3 nanoflakes, which is still limited by the high nucleation density and three-dimensional isotropic growth tendency. Herein, we propose a universal strategy of suppressing nucleation and slow-kinetic epitaxial growth of large domain 2D nonlayered β-In_2S_3 nanoflakes via water molecules for the optoelectronic applications. The water molecules acted as the function of partially oxidized In_2S_3 nucleus via mild oxidation, which reduced the nucleation density by approximately three orders of magnitude and enabled the formation of large-area single-crystal with an average domain size of 120 μm and a maximum size approaching 270 μm. The structural characteristics and electronic structures of our β-In_2S_3 samples characterized by various characterization techniques showed unique single-crystalline nature and modified Fermi level properties. Furthermore, the diverse nanostructures of β-In_2S_3 could be precisely tuned from triangular nanosheets to nanowires by controlling the growth conditions. The two-terminal β-In_2S_3 photodetectors exhibited excellent performance with a high photoresponsivity of 44 $A \cdot W^{-1}$ and a fast response speed with rise and decay times of 6 and 7 ms, respectively, revealing the superior physical properties of large domain 2D β-In_2S_3. This work provides a universal water-assisted strategy for synthesizing large-area 2D non-layered materials and paves the way for significant potential of high-quality large-scale single-crystalline β-In_2S_3 for advanced optoelectronic devices applications.

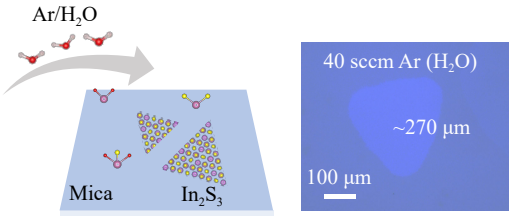

Keywords two-dimensional nonlayered β-In_2S_3, suppressing nucleation, slow-kinetic epitaxial growth, large domain size, optoelectronic devices

Higher Education Press

https://doi.org/10.15302/frontphys.2026.124201

1 Introduction

As a new family of 2D materials, nonlayered ultrathin nano-flakes have been successfully synthesized even down to the monolayer limits, resolving isotropic growth problems due to three-dimensional crystal structures [1–14], which demonstrate unique physicochemical properties such as monolayer ferroelectricity and piezoelectricity, new types of magnetism, high optoelectronic performance [3, 8, 14–16]. Indium sulfide (In_2S_3), a representative of III–VI chalcogenides with diverse polymorphism, is an attractive n-type semiconductor with potential applications in solar cells and flexible optoelectronics [13, 17–20]. In_2S_3 compounds could crystallize as tetragonal β-In_2S_3, cubic α-In_2S_3, and trigonal layered γ-In_2S_3, which can be distinguished by different ordered indium vacancies [21]. Among these polymorphs, the tetragonal β-phase is most thermodynamically stable at room temperature. Meanwhile, 2D β-In_2S_3 have shown tunable defects related band gaps, high absorption coefficient, and excellent photoresponsivity, indicating the great potential for optoelectronic devices application [22, 23]. Therefore, optoelectronic device applications of 2D β-In_2S_3 nanoflakes request controllable synthesis of high-quality and large domain-sizes samples, which could largely reduce electronic scattering effects to improve optoelectronic devices performance [24].

Early research on the synthesis of 2D In_2S_3 primarily focused on the solution-phase methods, achieving polycrystalline 2D In_2S_3 with surface defects and contaminations [24, 25]. Subsequently, a space-confined chemical vapor deposition (CVD) was developed using InI_3 and sulfur powders, which demonstrated the synthesis of 2D In_2S_3 nanoflakes with lateral size of ~10 μm and lowest thickness of 1.5 nm with broadband response for high quantum efficiency [26]. However, CVD-synthesized In_2S_3 nanoflakes are generally limited in domain size, which largely limits its further application. Recently, physical vapor deposition (PVD) was applied to achieve a rapid growth of single crystal In_2S_3 with largest domain size of ~160 μm and a thickness of 20 nm, showing broadband response from visible to near-infrared region [22, 27]. However, conventional PVD synthesis of 2D β-In_2S_3 nanostructures with large domain sizes remains a significant challenge, suffering from inherent three-dimensional bonds, and relatively weak In–S bond strength induced high volatility of the In_2S_3 powder, often leading to excessively high nucleation density and resulting in the formation of polycrystalline film with limited domain size and poor thickness control [28–30]. Despite the above problems, recent progress still needs to pave a significant gap towards large-scale synthesis of single-crystalline 2D In_2S_3 film.

Here, we aim to address the nucleation and epitaxial growth issues by employing H_2O vapor to control the nucleation density and achieve large domain size of 2D β-In_2S_3 nanoflakes. This water-assisted PVD strategy greatly reduces the nucleation sites of 2D β-In_2S_3, which also results in ultrathin nanoflakes with lateral size of 270 μm with the thickness of 3.6 nm. The H_2O assisted growth mechanism is also revealed as the elemental step controls of suppressed nucleation and slow-kinetic epitaxy. The fabricated large domain 2D β-In_2S_3 photodetectors exhibit reasonable photo-response characteristics and a fast response speed.

2 Experimental section

2.1 Preparation of β-In_2S_3 nanoflakes

2D β-In_2S_3 nanoflakes were synthesized on mica substrate in an atmospheric pressure physical vapor deposition (APPVD) system using In_2S_3 powder as precursor. Specifically, 20–50 mg of In_2S_3 powder (99.9%, Macklin) was placed in the central zone of a quartz tube furnace. Two freshly cleaved mica substrates were positioned in the downstream low-temperature region, located 12–15 cm away from the In_2S_3 precursor. Before growth, the system was purged with high-purity argon (200 sccm) for approximately 10 minutes to remove residual air. The furnace temperature was then heated to 850 °C and the growth time was maintained for 10 min. During the growth process, the argon carrier gas (20–60 sccm) was directed through a glass bottle filled with deionized water to introduce a controlled amount of water vapor into the reaction environment to actively participate in the chemical vapor deposition process. After reaction completion, the system was allowed to cool naturally to room temperature under continuous argon flow of 20–60 sccm without water vapor, preserving the structural integrity of the as-grown samples.

2.2 Transfer of 2D β-In_2S_3 nanoflakes

The 2D β-In_2S_3 nanoflakes were transferred onto copper grid or SiO_2 using polymethyl methacrylate (PMMA)-assisted wet transfer process for TEM and Raman characterization. The In_2S_3/mica substrate was spin-coated with a 1 wt% PMMA solution: 10 s at 500 rpm for uniformity, followed by 50 s at 4500 rpm to achieve a thin and consistent film. The sample was then baked at 140 °C for 20 minutes to solidify the PMMA for its adhesion to In_2S_3 nanoflakes. And then the sample was immersed in a 1 wt% HF solution, enabling the PMMA/β-In_2S_3 film to detach from the mica substrate. The released film was immersed in deionized water to remove residual HF, then carefully transferred to the target substrate and baked at 90 °C for 5 minutes. Finally, the remaining PMMA was removed by immersing in hot acetone and isopropanol alcohol (about 70 °C),

resulting in achieving clean β-In_2S_3 nanoflakes on the target substrates.

2.3 Characterization of 2D β-In_2S_3 nanoflakes

The optical microscope (OM, Olympus, BX53M) was used to obtain the surface morphology of our samples. The atomic force microscope (AFM, Oxford instruments, MPF-3D) equipped with scanning Kelvin Probe Force Microscopy (KPFM) was used to characterize micromorphology, thickness, and the surface potential of In_2S_3 nanowires or nanoflakes. The Raman spectrometer (Raman, Thermo Fisher Scientific, DXR3) with 532 nm laser as the excitation wavelength was used to characterize the phase of In_2S_3 samples. The transmission electron microscopy (TEM, FEI Tecnai F20) equipped with an energy dispersive X-ray (EDX) spectrometer was used to analyze the crystal structure and elemental composition of β-In_2S_3 nanoflakes, while selected-area electron diffraction data were also collected by the SAED module.

2.4 Fabrication and measurements of 2D β-In_2S_3 photodetectors

The device is fabricated via an Ultraviolet Maskless Lithography machine (TuoTuo Technology (Suzhou) Co., Ltd.). The electrodes were patterned on the β-In_2S_3 nanoflakes on mica substrates, and then metal films of In/Au (10/50 nm) were deposited by thermally evaporated deposition device (VNANO, VZZ-300S). The electrical and optoelectrical properties of β-In_2S_3 were characterized at room temperature using semiconductor analyzer system (PDA, FS-Pro) equipped with a probe station. The photodetector was illuminated with laser diodes at wavelengths of 520 nm and 650 nm and the incident optical power was measured using an optical power meter (Newport 843-R) to ensure reliable illumination conditions.

3 Results and discussion

Figure 1(a) shows the schematic of water-assisted growth strategy on mica substrate, in which high-purity In_2S_3 (~99.9%) powder was placed in the central zone of tube furnace. Two cleaved mica substrates were positioned at ~13–15 cm downstream from the In_2S_3 powder. High-purity argon (Ar) flow was introduced through a glass bottle containing deionized water, where the evaporated In and S clusters can mix with Ar-H_2O vapor, thereby participating in the nucleation and epitaxy processes (Fig. S1 of the Electronic Supplementary Materials). The Ar flow rate is directly proportional to the number of H_2O molecules, achieving the appropriate amount for tuning reaction kinetics. At room temperature, β-In_2S_3 has the covalent bonded nonlayered tetragonal structure, which belongs to the $I4_1/amd$ space group with lattice constants of $a = b = 7.68$ Å, $c = 32.62$ Å, and $\alpha = \beta = \gamma = 90°$ [Figs. 1(b) and S2] [21]. The atomic structure of $(10\bar{6})$ plane shows tetragonal symmetry with ordered vacancies, while the (103) plane belongs quasi-triple symmetric structure. Optical image (OM) of 2D In_2S_3 nanoflakes obtained under Ar-H_2O flow rate of 20 sccm is shown in Fig. 1(c), exhibiting nucleation density is two orders of magnitude lower than that of the samples grown without H_2O (detailed in Fig. S3). The pyramid domain morphology of In_2S_3 nanoflakes [Fig. 1(c)] indicates water molecules actively influence the reaction kinetics, promoting a quasi-layer-by-layer growth mechanism. Large domain size of ~270 μm 2D In_2S_3 nanoflakes [Fig. 1(d)] were obtained by optimizing growth parameters, which strongly confirms that the participation of H_2O facilitates larger In_2S_3 domains. Atomic force microscopy (AFM) characterization reveals the thickness can be controlled from 3.5 nm to 14.4 nm [Figs. 1(e) and S4], exhibiting uniform surface and high crystalline quality. Therefore, water molecules play an important role in suppressing nucleation and promoting lateral expansion of domains.

Raman spectrum of the water-assisted In_2S_3 exhibits four distinct peaks at 247, 309, 323, and 367 cm^{-1} [Fig. 1(f)]. The peaks at 247 cm^{-1} and 367 cm^{-1} can be assigned to A_{1g} vibrational modes of β-In_2S_3, while the Raman peaks at 309 cm^{-1} and 323 cm^{-1} correspond to E_g modes of β-In_2S_3 [22, 31, 32]. Meanwhile, thickness dependent Raman measurements were also conducted to characterize 2D β-In_2S_3 [Fig. 1(g)]. For ultrathin samples below 10 nm, only two characteristic peaks of A_{1g} (247 cm^{-1}) and A_{1g} (367 cm^{-1}) were observed, whereas the E_g vibrational mode at 309 and 323 cm^{-1} were suppressed. As the thickness increased, the peak around 315 cm^{-1} split into two distinct peaks, identified as the E_g (309 cm^{-1}) and E_g (321 cm^{-1}). To evaluate the structural stability of β-In_2S_3, we compared the Raman spectra of sample exposed to ambient and stored under vacuum for six months (Fig. S5). The spectrum of β-In_2S_3 exposed to ambient air shows an additional prominent peak emerges at around 130 cm^{-1}, which matches the characteristic Raman mode of In_2O_3 [33]. In contrast, the Raman spectrum of vacuum-stored sample does not exhibit noticeable peak shift. These results indicate that β-In_2S_3 maintains its structural stability when kept in a vacuum environment. Figure 1(h) presents X-ray photoelectron spectroscopy (XPS) analysis of the as-grown sample before and after six months of exposure to ambient air. For the freshly synthesized sample, the In 3d core-level spectrum exhibits two obvious peaks of 444.7 eV and 452.2 eV, corresponding to the In $3d_{5/2}$ and In $3d_{3/2}$, respectively, which shows the energy splitting (ΔE) of 7.5 eV in agreement with previously reported β-In_2S_3 [32, 34]. In addition, after air exposure for six months, the XPS spectrum exhibits two distinct peaks at 446.2

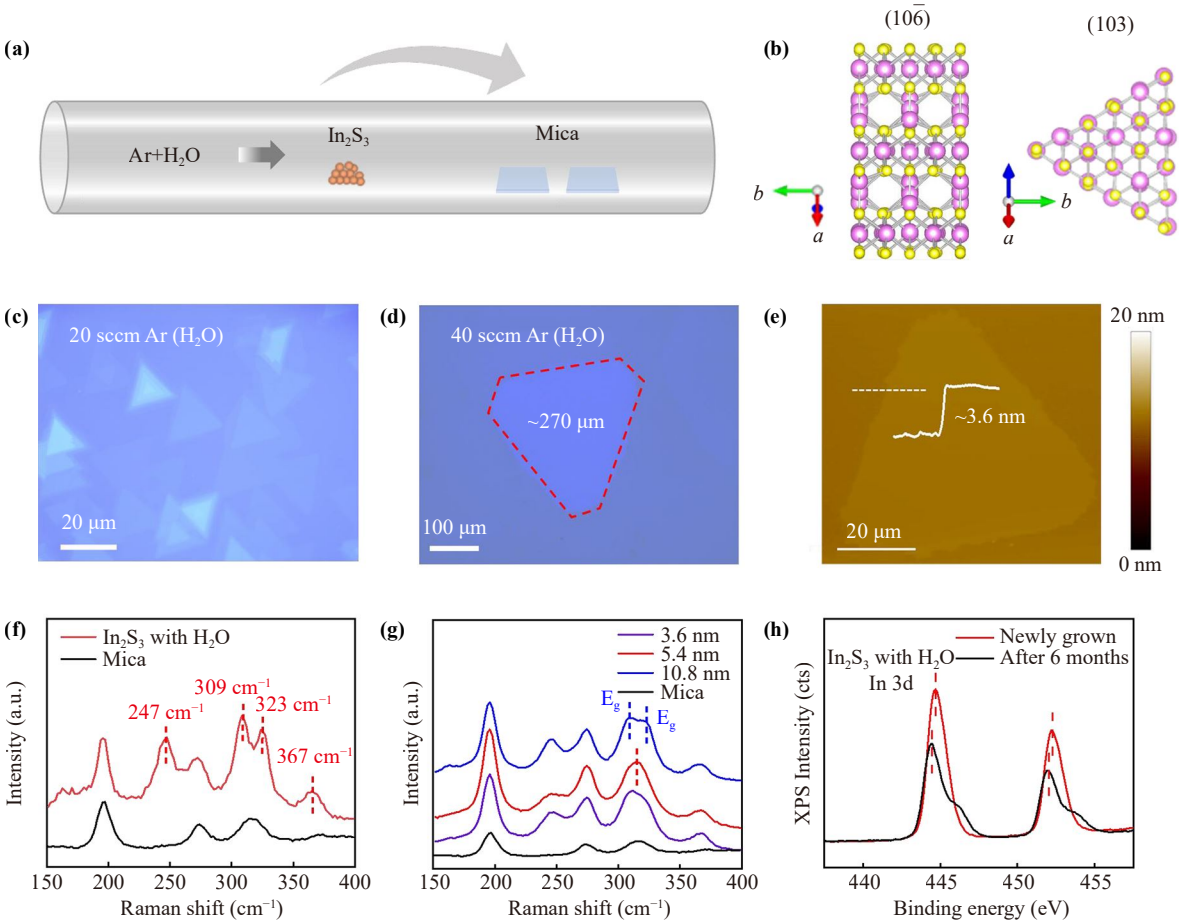

Fig. 1 **(a)** Schematic diagram of 2D β-In_2S_3 growth by water assisted PVD. **(b)** Atomic structure models of β-In_2S_3 (103) and (10$\bar{6}$) plane. **(c)** Optical image of 2D β-In_2S_3 grown under a 20 sccm Ar. **(d)** Optical image of large domain β-In_2S_3 with a lateral dimension of approximately 270 μm grown under a 40 sccm Ar. **(e)** AFM image of typical β-In_2S_3 with the thickness of 3.6 nm. **(f)** Raman spectrum of 2D β-In_2S_3 on mica substrate. **(g)** Raman spectrum of 2D β-In_2S_3 for different thicknesses. **(h)** X-ray photoelectron spectroscopy (XPS) energy spectra of In 3d peaks for β-In_2S_3.

and 453.7 eV, indicating surface oxidation after long time air exposure leads to the weak formation of In–O bonds and its reasonable stability [34, 35]. Therefore, the water-assisted grown In_2S_3 samples are clearly identified as the β-phase and exhibit high purity and excellent crystalline quality. Moreover, XPS spectra for In 3d reveal a higher binding energy for the water assisted grown In_2S_3 nanoflakes compared to the sample stored for 6 months, indicating a potential modified surface environment with trace In–O bonding. This shift aligns with the higher electronegativity of oxygen relative to sulfur.

Transmission electron microscopy (TEM) and selected-area electron diffraction (SAED) were employed to characterize crystalline microstructure and chemical composition of β-In_2S_3 samples, which were transferred onto copper grids using wet chemical etching method [8]. High-resolution TEM (HRTEM) image revealed the clear lattice fringe of 3.9 Å, which was indexed as the distance of (020) plane for β-In_2S_3 [Fig. 2(a)]. The corresponding SAED pattern [Fig. 2(b)] displays a hexagonal symmetric diffraction spot, matching well with the simulated diffraction along the [601] zone axis [Fig. 2(c)] and confirming single crystalline structure with quasi-triple symmetry. The elemental energy-dispersive X-ray spectroscopy (EDS) maps of In and S elements showed uniform distribution of In and S elements across the In_2S_3 nanoflake [Figs. 2(e) and (f)], respectively, which correspond to the area outlined in low-magnification TEM image [Fig. 2(d)]. The analysis of the EDS spectrum yields an atomic ratio of In to S approximately 39.7:60.3 (Fig. S6), which further confirms the high chemical purity and correct stoichiometry of our samples. The SAED pattern is indexed to the [601] zone axis, which is perpendicular to the (020) plane. By understanding theoretical atomic structure of β-In_2S_3 [Fig. 2(g)], the crystallographic orientation relative to the substrate can be unambiguously determined, finally revealing the horizontal growth plane corresponds to the (103) crystal plane.

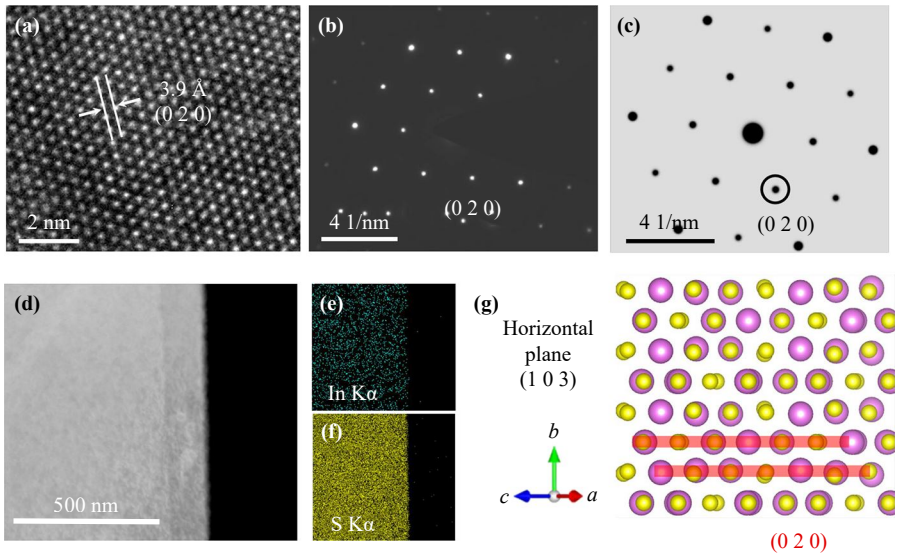

Fig. 2 **(a)** HRTEM image of β-In_2S_3 nanoflake. **(b)** SAED collected from (a). **(c)** Simulated diffraction pattern of single crystal β-In_2S_3 along [601] axis zone. **(d)** Low-magnification TEM image of β-In_2S_3 nanoflake. **(e, f)** EDS mapping of In and S elemental of β-In_2S_3 flake in (d). Scale bar is 500 nm. **(g)** Atomic model structure along [601] axis orientation (In atoms, purple; S atoms, yellow).

Figure 3(a) shows the proposed schematic of water-assisted growth mechanism. As supported by prior studies, H_2O molecules can act as a mildly partial oxidizing agent at high temperature [36]. Herein, we propose that the introduction of H_2O molecules can oxidize partial In–S clusters, inhibiting their function as active epitaxial growth centers and thereby dramatically reducing the overall nucleation density. The precursor flux is concentrated on the limited number of nucleus active sites, promoting lateral expansion via a slow kinetic process and enabling the formation of large-domain 2D β-In_2S_3 nanoflakes. The XPS results confirm that the mild oxidizing property of H_2O molecules does not completely oxidize In–S bonds into In–O bonds during the epitaxy process [37]. Therefore, H_2O molecules act as the passivators that prevent large number of In–S clusters becoming epitaxial centers during the nucleation stage, which largely reduces nucleation densities and expands the domain size.

To elucidate the water-assisted growth mechanism, a series experiments were conducted to investigate the influence of critical parameters. The morphological evolution of 2D β-In_2S_3 was achieved by controlling Ar flow rate to modulate the growth kinetics in different atmospheres with and without H_2O (Figs. 3 and S7). The optical images of β-In_2S_3 grown with H_2O at Ar flow rates from 20 to 60 sccm at 600 °C are shown in Figs. 3(b)–(d). As the effective supply of H_2O molecules enhanced, the average lateral domain size expanded from approximately 5 μm to 80 μm. Meanwhile, the estimated nucleation densities decreased from 7.1×10^8 m^{-2} to 3.3×10^7 m^{-2} [Fig. 3(e)]. In contrast, we evaluated the results of 2D β-In_2S_3 grown in pure Ar gas under identical growth conditions. Although the nucleation density experienced a slight decrease from 7.7×10^{11} m^{-2} to 2.2×10^{10} m^{-2} with increased flow rate, it remains at a relatively higher order of magnitude [Figs. 3(f)–(h)], also showing the restricted domain size of ~20 μm. Further epitaxial growth results in the formation of polycrystalline films with diverse grain boundaries and defects. To further check the general influence of H_2O molecules, we conducted similar experiments on C-sapphire substrates. AFM image of β-In_2S_3 (Fig. S8) grown without H_2O showed high nucleation density with domain sizes of ~500 nm. When H_2O molecules were introduced into the atmosphere, the average domain size increased to 4–6 μm. These findings confirm that the general applicability of water-assisted strategy of synthesizing large-domain 2D β-In_2S_3 on diverse substrates.

The optical images of In_2S_3 samples grown at the temperature of 500 °C, 550 °C, and 600 °C for 10 minutes were shown in Figs. 4(a)–(c), respectively. At 600 °C, the β-In_2S_3 exhibits regular triangular crystalline domain [Fig. 4(a)]. When the temperature decreased to 550 °C, one-dimensional nanowire structures coexisted with the nanoflake morphology [Fig. 4(b)]. As the growth temperature further reduced to 500 °C, the dominant morphology of samples shifted to nanowires [Fig. 4(c)]. The grown results within the temperature range of 550–600 °C are presented in Fig. S9, exhibiting a more clearly transition process. This morphological evolution may be attributed to modified kinetic control at lower temperatures, which promotes the rapid deposition of In_2S_3 on specific crystal planes. At the high temperature, In–S atoms or clusters on the substrate possess higher mobility. Therefore, the growth process is ther-

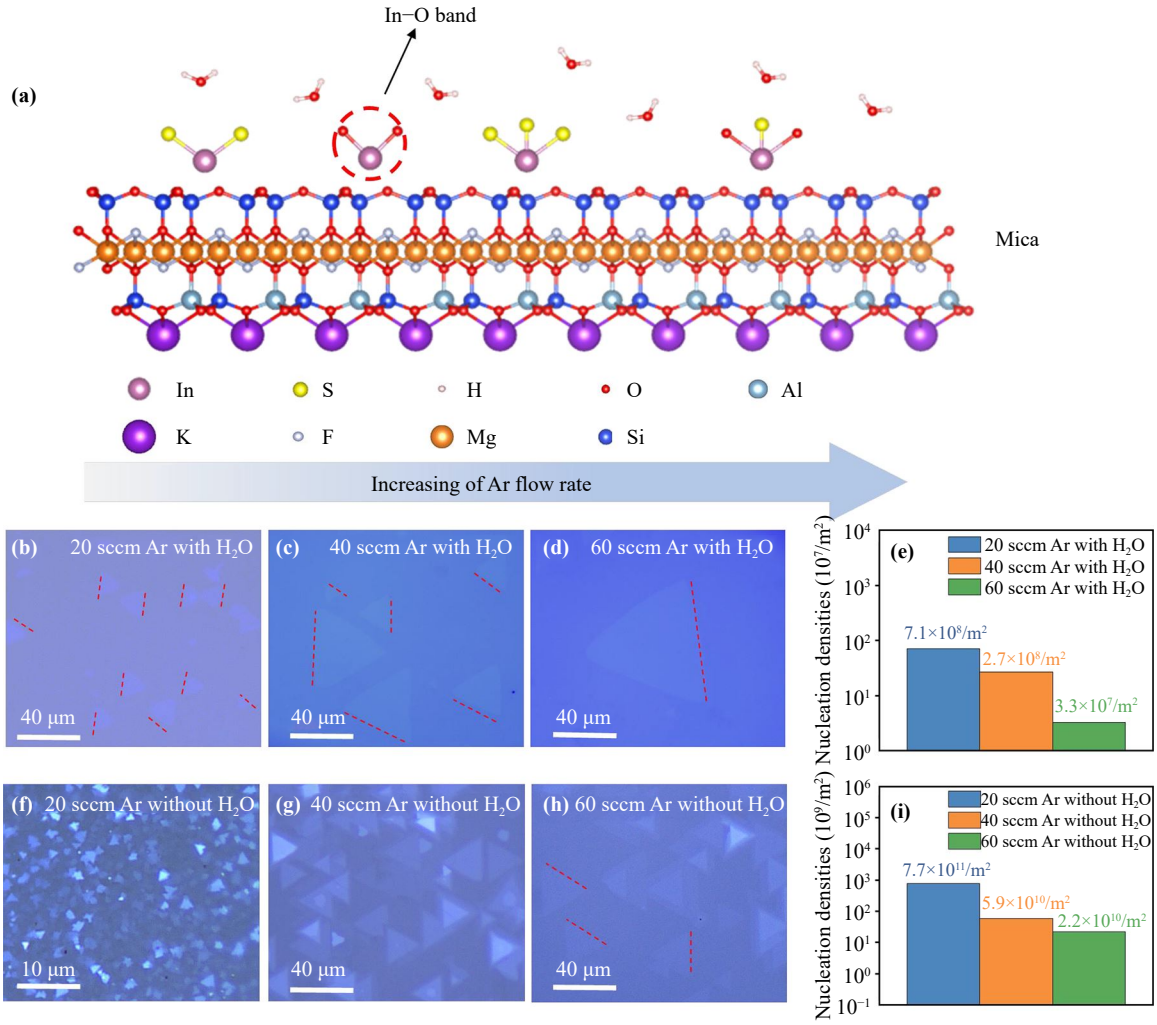

Fig. 3 **(a)** Schematic illustration for the H_2O-assisted growth mechanism. **(b–d)** OM images of In_2S_3 obtained at Ar-H_2O flow rate of 20 sccm (b), 40 sccm (c), 60 sccm (d), respectively. **(e)** Corresponding nucleation densities under H_2O growth conditions. **(f–h)** OM images of In_2S_3 obtained in pure Ar atmosphere of 20 sccm (f), 40 sccm (g), 60 sccm (h), respectively. (i) Corresponding nucleation densities under H_2O growth conditions.

modynamically driven towards the formation of 2D nanoflakes, which represent the structure with lowest surface energy for the crystal orientation [3]. Conversely, at the low temperature, the diffusion ability of atoms or clusters is significantly limited, thus hindering the formation of 2D structure. Instead, atoms preferentially migrate to dangling bonds or defect sites on nanowires, leading to the deposition of specific crystal direction [38–41]. Figure 4(d) shows Raman spectrum of In_2S_3 nanowires on the SiO_2 substrate. Three distinct characteristic peaks are observed at A_{1g} (247 cm^{-1}), E_g (309 cm^{-1}), and A_{1g} (367 cm^{-1}), which are identical to β-In_2S_3 nanoflakes [Fig. 1(f)]. With the growth temperature fixed at 500 °C, the influence of Ar flow rate (with H_2O) on the nanowire growth was examined. As the flow rate increased from 20 to 60 sccm, the nucleation densities of β-In_2S_3 nanowires dramatically decreased by 1–2 orders of magnitude, while the maximum length of nanowires increased to ~100 μm [Figs. 4(e)–(g)]. This finding further confirms the nucleation suppression by H_2O molecules, which is consistent with our observations in the In_2S_3 nanoflake (Fig. 3). As depicted in Fig. 4(h), the AFM image and corresponding height profile of the In_2S_3 nanowire reveal a uniform nanowire morphology with a thickness of ~60 nm (Fig. S10), demonstrating well-defined structural integrity.

To investigate the optoelectronic properties of large domain 2D β-In_2S_3 nanoflakes grown with H_2O, roomtemperature electrical transport measurements were carried out. We constructed two-terminal β-In_2S_3 photodetectors on mica substrate, the schematic device configuration of which is shown in Fig. 5(a). The electrodes were patterned via direct-writing ultraviolet lithography equipment, followed by the deposition of 10 nm In and 50 nm Au layers as contact electrodes. The channel length was controlled to be ~6 μm. Figure 5(b) shows

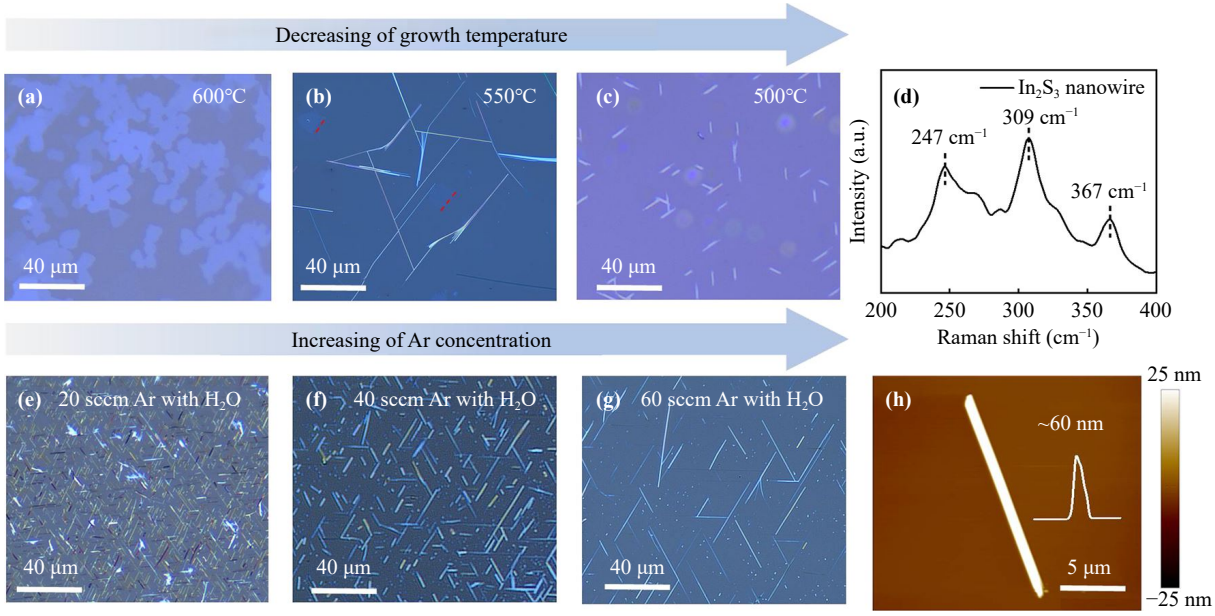

Fig. 4 **(a–c)** OM images of In_2S_3 obtained at different growth temperatures of 600 (a), 550 (b), and 500 °C (c), respectively. **(d)** Raman spectrum of In_2S_3 nanowires on SiO_2 substrate. **(e–g)** OM images of In_2S_3 nanowire obtained at different Ar-H_2O flowing rates at 500 °C. **(h)** AFM image of a β-In_2S_3 nanowire with the thickness of approximate 60 nm.

the differences of surface potential between In_2S_3 grown with H_2O and without H_2O, as measured by Au-referenced scanning Kelvin Probe Force Microscopy (KPFM). The results indicate that the work function of β-In_2S_3 nanoflakes grown with H_2O is 0.08 eV lower than that of β-In_2S_3 nanoflakes grown without H_2O, confirming a shift of the Fermi level toward a more intrinsic position [Figs. S11 and S12]. The surface potential mappings [Fig. 5(b)] suggest the different surface environments between two sample types. The current voltage (I–V) characteristics of β-In_2S_3 photodetector were measured under 650 nm laser illumination with different optical powers. The I–V curves demonstrate obvious rectification behavior within the voltage range of –2.5 V to 2.5 V [Fig. 5(c)], suggesting the Schottky contact at the semiconductor-electrode interface [42]. When the incident power increased from dark states to 0.67 nW, the photocurrent (V_{ds} = 2.5 V) increased from 1.5 nA to 25.7 nA. The R_λ increases nearly linearly with the increasing optical power [Fig. 5(d)], reaching a maximum R_λ of 44 $A \cdot W^{-1}$ at an incident power of 0.07 nW and a bias voltage of 2 V [43].

The temporal photocurrent of the device was evaluated under 520 nm illumination at a bias of 1 V. Figure 5(e) shows the time-resolved photocurrent curve of the β-In_2S_3 photodetector measured at different power densities. As the light power density increased from 59 $mW \cdot cm^{-2}$ to 147 $mW \cdot cm^{-2}$, the photocurrent rose from about 0.1 nA to 0.25 nA, demonstrating a clear positive correlation with high photosensitivity. However, when the power density further increased to 232 $mW \cdot cm^{-2}$, a reduction in the photocurrent is observed. This reduction can be attributed to the rapid saturation of trap states under strong illumination, which may limit efficient carrier generation and result in a lower photocurrent. All measured photocurrent curves exhibit stable, uniform, and highly reproducible switching characteristics over multiple cycles, demonstrating the robust and reliable photo-response stability of the β-In_2S_3 device. Figure 5(f) shows the response speed of the β-In_2S_3 device under 520 nm illumination, where the rise time (τ_{rise}) and decay time (τ_{decay}) are estimated to be ~ 6 ms and 7 ms, respectively. Compared to previous reports, our β-In_2S_3 sample exhibits a faster response time and excellent performance (Table S1). The energy band diagram under different states were schematically presented in Figs. 5(g)–(i). Figure 5(g) shows the band structure of the metal electrode prior to contact with the semiconductor. The Fermi level of β-In_2S_3 is approximately 4.75 eV, which is slightly higher than the work function of the In electrode (4.1 eV), inducing downward band bending at the interface and leading to the Schottky barrier [Fig. 5(h)]. The unequal contact areas of source and drain electrodes result in the formation of unbalanced charge injection effects [Fig. 5(b)], which contributes to final rectification characteristics. Under external bias and light illumination, photogenerated electron–hole pairs are driven in opposite directions across the Schottky barrier, thereby generating photocurrent under the bias [Fig. 5(i)]. In addition, the abundant trap states allow the capture of the photogenerated excitons by defect-related energy levels, resulting in prolonged carrier lifetimes and enhanced photo-response performance. Therefore, this work provides the mechanism understanding of 2D

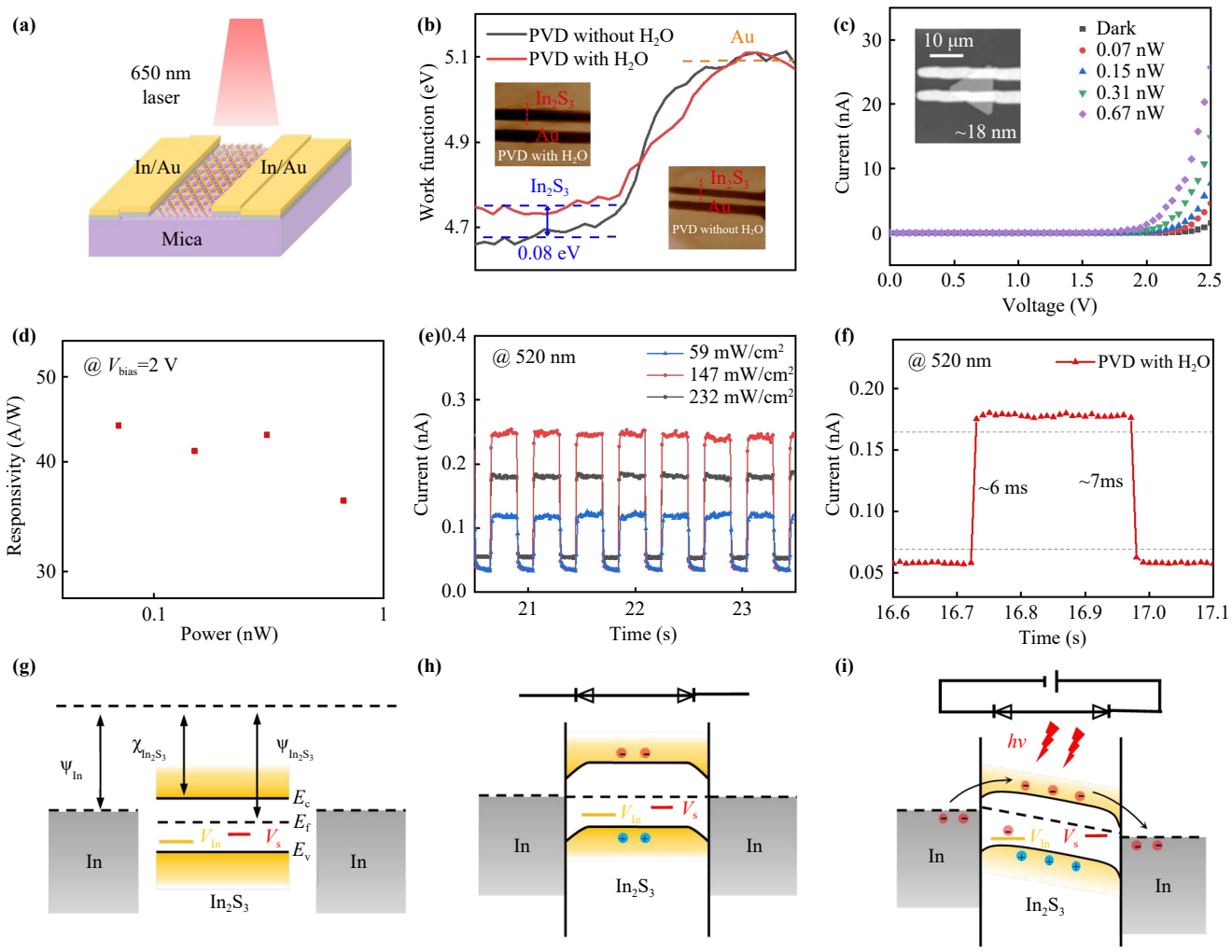

Fig. 5 **(a)** Schematic of the β-In_2S_3 photodetector. **(b)** Work functions comparison of Au and β-In_2S_3 nanoflakes grown with (or without) H_2O. Inset: Corresponding surface potential mapping images of β-In_2S_3 devices. **(c)** *I*–*V* characteristic curves of the β-In_2S_3 photodetector under illuminations of 650 nm at different light power. Inset: OM image of typical β-In_2S_3 (grown with H_2O) device. **(d)** Plots of responsivity of photodetector under different light power at the bias of 2 V. **(e)** Time-resolved photocurrent response of the β-In_2S_3 photodetector under different light power at the bias of 1 V under 520 nm illumination. **(f)** Rise and decay response time extracted from (e). **(g–i)** Energy band structure diagram of β-In_2S_3 photodetector before contact (g), after contact without bias voltage (h), and after contact with bias voltage and illumination (i), respectively.

β-In_2S_3 photodetectors and the potential for large-scale integration in optoelectronic applications [44, 45].

4 Conclusion

In this study, high-quality 2D single-crystal β-In_2S_3 nanoflakes were synthesized via water-assisted PVD strategy. The mild oxidation of H_2O vapor effectively passivates In–S clusters, thereby inhibiting the nucleation density of In_2S_3 by three orders of magnitude and enabling the formation of large-area single crystals with a maximum size approaching 270 μm. Photodetectors based on water-assisted grown β-In_2S_3 exhibited excellent performance, including a high photoresponsivity of 44 $A \cdot W^{-1}$ and a fast response speed with rise and decay times of 6 and 7 ms, respectively. In conclusion, this work provides a new strategy for synthesizing large domain 2D non-layered materials for advanced optoelectronic devices applications.

Declarations The authors declare that they have no competing interests and there are no conflicts.

Electronic supplementary materials The online version contains supplementary material available at https://doi.org/10.15302/frontphys.2026.124201.

Acknowledgements This work was financially supported by the National Natural Science Foundation of China (U23A20570), the Science and Technology Innovation Program of Hunan Province (2025RC1015). This work was also supported by State Key Laboratory of Precision Measuring Technology and Instruments (Tianjin University). This work was supported by Double Cs-corrected TEM Laboratory of the State Key Laboratory of Powder Metallurgy.

References

1. K. Chang, J. Liu, H. Lin, N. Wang, K. Zhao, A. Zhang, F. Jin, Y. Zhong, X. Hu, W. Duan, Q. Zhang, L. Fu, Q. K. Xue, X. Chen, and S. H. Ji, Discovery of robust in-plane ferroelectricity in atomic-thick SnTe, *Science* 353(6296), 274 (2016)
2. Y. Wu, J. Zheng, Q. Li, M. Song, S. Yue, N. Lin, and L. Jiao, Synthesis of superconducting two-dimensional non-layered PdTe by interfacial reactions, *Nat. Synth.* 1(11), 908 (2022)
3. B. Li, Z. Wan, C. Wang, P. Chen, B. Huang, X. Cheng, Q. Qian, J. Li, Z. Zhang, G. Sun, B. Zhao, H. Ma, R. Wu, Z. Wei, Y. Liu, L. Liao, Y. Ye, Y. Huang, X. Xu, X. Duan, W. Ji, and X. Duan, Van der Waals epitaxial growth of air-stable $CrSe_2$ nanosheets with thickness-tunable magnetic order, *Nat. Mater.* 20(6), 818 (2021)
4. X. Guo, X. Zhou, W. Chu, X. Fan, C. Li, L. Zou, C. Niu, B. Zhang, Y. Lu, H. Zhang, F. OuYang, Z. Wu, and Y. Zhou, Remote vapor-phase dual alkali halide salts assisted quasi-van der Waals epitaxy of m-phase ZrO_2 thin films with high dielectric constant and stable flexible properties, *Appl. Phys. Lett.* 125(8), 084101 (2024)
5. X. Fan, L. Zou, W. Chu, L. Wang, and Y. Zhou, Synthesis of high resistive two-dimensional nonlayered Cr_2S_3 nanoflakes with stable phosphorus dopants by chemical vapor deposition, *Appl. Phys. Lett.* 122(22), 222101 (2023)
6. X. Fan, J. Yi, B. Deng, C. Zhou, Z. Zhang, J. Yu, W. Li, C. Li, G. Wu, X. Zhou, T. Sun, Y. Zhu, J. Zhou, J. Xia, Z. Wang, K. Lai, Z. Peng, D. Li, A. Pan, and Y. Zhou, 2D edge-seeded heteroepitaxy of ultrathin high-κ dielectric $CaNb_2O_6$ for 2D field-effect transistors, *Nat. Commun.* 16(1), 2586 (2025)
7. W. Chu, R. Xin, L. Zou, X. Fan, X. Zhou, C. Li and Y. Zhou, Synthesis of nonlayered 2D α-Fe_2O_3 nanosheets by ultralow concentration precursor with Se catalysts design, *Phys. Status Solidi RRL.* 18(7), 2300102 (2023)
8. H. Chen, Z. Tian, X. Zhou, X. Fan, Z. Li, C. Li, C. Niu, W. Chu, Y. Zhou, L. He, Y. Yang, Z. Peng, and Y. Zhou, Approaching charge compensation limit for promoting magnetoresistance in 2D nonlayered MoO_2 via surface hydrogen passivation, *Adv. Funct. Mater.* 35(22), 242204 (2025)
9. J. Shen, Y. Xie, and J. J. Cha, Revealing surface states in In-doped SnTe nanoplates with low bulk mobility, *Nano Lett.* 15(6), 3827 (2015)
10. J. Shen, Y. Jung, A. S. Disa, F. J. Walker, C. H. Ahn, and J. J. Cha, Synthesis of SnTe nanoplates with {100} and {111} surfaces, *Nano Lett.* 14(7), 4183 (2014)
11. N. Syed, A. Zavabeti, K. A. Messalea, E. Della Gaspera, A. Elbourne, A. Jannat, M. Mohiuddin, B. Y. Zhang, G. Zheng, L. Wang, S. P. Russo, D. Esrafilzadeh, C. F. McConville, K. Kalantar-Zadeh, and T. Daeneke, Wafer-sized ultrathin gallium and indium nitride nanosheets through the ammonolysis of liquid metal derived oxides, *J. Am. Chem. Soc.* 141(1), 104 (2019)
12. Y. Chen, K. Liu, J. Liu, T. Lv, B. Wei, T. Zhang, M. Zeng, Z. Wang, and L. Fu, Growth of 2D GaN single crystals on liquid metals, *J. Am. Chem. Soc.* 140(48), 16392 (2018)
13. F. Horani and E. Lifshitz, Unraveling the growth mechanism forming stable γ-In_2S_3 and β-In_2S_3 colloidal nanoplatelets, *Chem. Mater.* 31(5), 1784 (2019)
14. C. Gong, J. Chu, C. Yin, C. Yan, X. Hu, S. Qian, Y. Hu, K. Hu, J. Huang, H. Wang, Y. Wang, P. Wangyang, T. Lei, L. Dai, C. Wu, B. Chen, C. Li, M. Liao, T. Zhai, and J. Xiong, Self-confined growth of ultrathin 2D nonlayered wide-bandgap semiconductor CuBr flakes, *Adv. Mater.* 31(36), 1903580 (2019)
15. C. Chang, W. Chen, Y. Chen, Y. Chen, Y. Chen, F. Ding, C. Fan, H. Jin Fan, Z. Fan, C. Gong, Y. Gong, Q. He, X. Hong, S. Hu, W. Hu, W. Huang, Y. Huang, W. Ji, D. Li, L. J. Li, Q. Li, L. Lin, C. Ling, M. Liu, N. Liu, Z. Liu, K. Ping Loh, J. Ma, F. Miao, H. Peng, M. Shao, L. Song, S. Su, S. Sun, C. Tan, Z. Tang, D. Wang, H. Wang, J. Wang, X. Wang, X. Wang, A. T. S. Wee, Z. Wei, Y. Wu, Z. S. Wu, J. Xiong, Q. Xiong, W. Xu, P. Yin, H. Zeng, Z. Zeng, T. Zhai, H. Zhang, H. Zhang, Q. Zhang, T. Zhang, X. Zhang, L. D. Zhao, M. Zhao, W. Zhao, Y. Zhao, K. G. Zhou, X. Zhou, Y. Zhou, H. Zhu, H. Zhang, and Z. Liu, Recent progress on two-dimensional materials, *Acta Phys. Chim. Sin.* 37(12), 2108017 (2021)
16. B. Jin, P. Huang, Q. Zhang, X. Zhou, X. Zhang, L. Li, J. Su, H. Li, and T. Zhai, Self-limited epitaxial growth of ultrathin nonlayered CdS flakes for high-performance photodetectors, *Adv. Funct. Mater.* 28(20), 1800181 (2018)
17. W. Chu, X. Zhou, Z. Wang, X. Fan, X. Guo, C. Li, J. Yue, F. Ouyang, J. Zhao, and Y. Zhou, Stable alkali halide vapor assisted chemical vapor deposition of 2D $HfSe_2$ templates and controllable oxidation of its heterostructures, *Front. Phys. (Beijing)* 19(3), 33212 (2024)
18. X. Fan, R. Xin, L. Li, B. Zhang, C. Li, X. Zhou, H. Chen, H. Zhang, F. OuYang, and Y. Zhou, Progress in the preparation and physical properties of two-dimensional Cr-based chalcogenide materials and heterojunctions, *Front. Phys. (Beijing)* 19(2), 23401 (2024)
19. P. Wang, W. Xue, J. Zeng, W. Ci, Q. Chen, B. Lv, R. Yang, Y. Liu, G. Liu, and X. Xu, Wavelength-selective photodetector and neuromorphic visual sensor utilizing intrinsic defect semiconductor, *Adv. Funct. Mater.* 34(46), 2407746 (2024)
20. Y. Zhou, D. Wu, Y. Zhu, Y. Cho, Q. He, X. Yang, K. Herrera, Z. Chu, Y. Han, M. C. Downer, H. Peng, and K. Lai, Out-of-plane piezoelectricity and ferroelectricity in layered α-In_2Se_3 nanoflakes, *Nano Lett.* 17(9), 5508 (2017)
21. P. Pistor, J. M. Merino Álvarez, M. León, M. di Michiel, S. Schorr, R. Klenk, and S. Lehmann, Structure reinvestigation of α-, β- and γ-In_2S_3, *Acta Crystallogr. B*

72(3), 410 (2016)
22. Y. Zhao, D. Yu, J. Lu, L. Tao, Z. Chen, Y. Yang, A. Wei, L. Tao, J. Liu, Z. Zheng, M. Hao, and J. B. Xu, Thickness-dependent optical properties and In-plane anisotropic Raman response of the 2D β-In_2S_3, *Adv. Opt. Mater.* 7(22), 1901085 (2019)
23. J. Zhu, S. Wu, L. Wang, J. Wu, J. Zhu, L. Zou, F. Xiao, Z. Su, C. Jiao, S. Pei, Z. Zhang, J. Qin, B. Xu, Y. Zhou, J. Xia, and Z. Wang, Broad-range, high-linearity, and fast-response pressure sensing enabled by nanomechanical resonators based on 2D non-layered material: β-In_2S_3, *InfoMat* 6(8), e12553 (2024)
24. S. Sarkar, A. D. P. Leach, and J. E. Macdonald, Folded nanosheets: A new mechanism for nanodisk formation, *Chem. Mater.* 28(12), 4324 (2016)
25. W. Wang, Z. Chen, X. Sui, Y. Li, X. Liu, and Y. Zhang, Phase/size dual controlled 2D semiconductor In_2X_3 (X = S, Se, Te) for saturable absorption modulation, *Nano Res.* 15(6), 5633 (2022)
26. C. L. Tu, K. I. Lin, J. Pu, T. F. Chung, C. N. Hsiao, A. C. Huang, J. R. Yang, T. Takenobu, and C. H. Chen, CVD growth of large-area InS atomic layers and device applications, *Nanoscale* 12(17), 9366 (2020)
27. J. Lu, Z. Zheng, W. Gao, J. Yao, Y. Zhao, Y. Xiao, B. Wang, and J. Li, Epitaxial growth of large-scale In_2S_3 nanoflakes and the construction of a high performance In_2S_3/Si photodetector, *J. Mater. Chem. C* 7(39), 12104 (2019)
28. N. Kaur, D. Sharma, and B. R. Mehta, Growth of In_2S_3 nanolayers on F-Mica, SiO_2, ZnO, and TiO_2 substrates using chemical vapor deposition, *Mater. Sci. Eng. B* 264, 114889 (2021)
29. D. Yu, Z. Zhuo, A. Wei, J. Liu, Y. Zhao, and Z. Xiao, Growth of large-area two-dimensional non-layered β-In_2S_3 continuous thin films and application for photodetector device, *J. Mater. Sci. Mater. Electron.* 31(20), 18175 (2020)
30. K. Zhang, Y. She, X. Cai, M. Zhao, Z. Liu, C. Ding, L. Zhang, W. Zhou, J. Ma, H. Liu, L. J. Li, Z. Luo, and S. Huang, Epitaxial substitution of metal iodides for low-temperature growth of two-dimensional metal chalcogenides, *Nat. Nanotechnol.* 18(5), 448 (2023)
31. Y. Chen, Z. Huang, Y. You, T. Jiang, H. Wu, Z. Zheng, C. Du, K. Chen, and T. Lai, Thickness-dependent optical properties and ultrafast carrier dynamics of 2D non-layered β-In_2S_3, *APL Mater.* 13(2), 021105 (2025)
32. W. Huang, L. Gan, H. Yang, N. Zhou, R. Wang, W. Wu, H. Li, Y. Ma, H. Zeng, and T. Zhai, Controlled synthesis of ultrathin 2D β-In_2S_3 with broadband photoresponse by chemical vapor deposition, *Adv. Funct. Mater.* 27(36), 1702448 (2017)
33. N. Zhao, X. Chang, X. Liu, J. Li, W. Zheng, and J. Zhang, Probing the structural dynamics of In_2O_3 using in situ raman spectroscopy: Bridging material dynamics and sensor functionality, *Angew. Chem. Int. Ed.* 64(45), e202512808 (2025)
34. K. Wang, Y. Hu, X. Liu, J. Li, and B. Liu, Visible-light-driven CO_2 photoreduction over atomically strained indium sites in ambient air, *Nat. Commun.* 16(1), 2094 (2025)
35. A. Kyndiah, A. Ablat, S. Guyot-Reeb, T. Schultz, F. Zu, N. Koch, P. Amsalem, S. Chiodini, T. Yilmaz Alic, Y. Topal, M. Kus, L. Hirsch, S. Fasquel, and M. Abbas, A multifunctional interlayer for solution processed high performance indium oxide transistors, *Sci. Rep.* 8(1), 10946 (2018)
36. P. Li and J. Zhang, Sorting out semiconducting single-walled carbon nanotube arrays by preferential destruction of metallic tubes using water, *J. Mater. Chem.* 21(32), 11815 (2011)
37. A. Cohen, A. Patsha, P. K. Mohapatra, M. Kazes, K. Ranganathan, L. Houben, D. Oron, and A. Ismach, Growth-etch metal–organic chemical vapor deposition approach of WS_2 atomic layers, *ACS Nano* 15(1), 526 (2021)
38. Q. Su, C. K. Huang, Y. Wang, Y. C. Fan, B. A. Lu, W. Lan, Y. Y. Wang, and X. Q. Liu, Formation of vanadium oxides with various morphologies by chemical vapor deposition, *J. Alloys Compd.* 475(1–2), 518 (2009)
39. Q. Su, X. Pan, E. Xie, Y. Wang, J. Qiu, and X. Liu, Influence of temperature on the microstructure of V_2O_5 film prepared by DC magnetron sputtering, *Rare Met.* 25(6 Suppl. 1), 82 (2006)
40. X. Xie and G. Shen, Single-crystalline In_2S_3 nanowire-based flexible visible-light photodetectors with an ultra-high photoresponse, *Nanoscale* 7(11), 5046 (2015)
41. B. Zhang, C. Niu, W. Chu, X. Guo, X. Zhou, C. Li, X. Fan, L. Zou, Z. Wu, Y. Lu, F. OuYang, Y. Zhou, and H. Zhang, Synthesis of 2D nonlayered α-Nb_2O_5 nanosheets by the growth promoter of sulfur and alkali halides, *Phys. Status Solidi RRL.* 18(8), 2400054 (2024)
42. W. Wu, L. Wang, R. Yu, Y. Liu, S. H. Wei, J. Hone, and Z. L. Wang, Piezophototronic effect in single-atomic-layer MoS_2 for strain-gated flexible optoelectronics, *Adv. Mater.* 28(38), 8463 (2016)
43. S. R. Tamalampudi, Y. Y. Lu, R. Kumar U., R. Sankar, C. D. Liao, K. M. B, C. H. Cheng, F. C. Chou, and Y. T. Chen, High performance and bendable few-layered InSe photodetecters with broad spectral response, *Nano Lett.* 14(5), 2800 (2014)
44. T. Zhu, Y. Zhang, X. Wei, M. Jiang and H. Xu, The rise of two-dimensional tellurium for next-generation electronics and optoelectronics, *Front. Phys. (Beijing)* 18(3), 33601 (2023)
45. B. Liu, W. Chu, S. Liu, Y. Zhou, L. Zou, J. Fu, M. Liu, X. Fu, F. Ouyang, and Y. Zhou, Engineering the nanostructures of solution proceed $In_2Se_xS_{3-x}$ films with enhanced near-infrared absorption for photoelectrochemical water splitting, *J. Phys. D* 55(43), 434004 (2022)